# An application of the scale-adapted simulation to the unsteady flow across a tube bundle

Mauro Grioni, Pascal Bruel, Sergio A Elaskar, Anibal E Mirasso

# An application of the scale-adapted simulation to the flow across a tube bundle

Mauro Grioni[†1,2], Pascal Bruel[3], Sergio A. Elaskar[1,4,5], and Anibal E. Mirasso[2]

[1]National Scientific and Technical Research Council, CONICET, Argentina

[2]Institute of Structural Mechanics and Seismic Risk, Faculty of Engineering, National University of Cuyo, Mendoza, 5500, Argentina

[3]CNRS - University Pau & Pays Adour, LMAP, Inria Cagire Team, Avenue de l'Université, 64013 Pau, France

[4]Department of Aeronautical, National University of Córdoba, Córdoba, 5000, Argentina

[5]Institute of Advanced Studies in Engineering and Technology (IDIT), CONICET - UNC, Argentina

**Abstract**

In the last decades, one of the main objectives pursued in the field of computational fluid dynamics has been the development of turbulent flow models and simulations techniques capable of generating predictions of flow patterns accurate enough to many industrial applications in a reasonable wall-clock time and at an acceptable cost. Very often, a trade-off has to be sought between the engineer's expectations regarding the accuracy of the model and the limited computational resources available. In that framework, the present contribution aims at demonstrating the capabilities of the SST-SAS approach which is considered as an intermediate model with respect to accuracy and computational requirements. To that end, the turbulent flow through a tube bundle was selected as test case. Preliminary sensitivity analyses were carried out to properly choose the residuals tolerance level, duration of the physical time integration, mesh size and time step value. The SST-SAS results are compared with available experimental data as well as with different simulations results taken from the literature. A quantitative scoring criterion was defined to sort out the different models results: the SST-SAS ranked first.

**Keywords**: Staggered tube bundle; SAS turbulence model; Reynolds stress tensor.

# 1 Introduction

Supposed to replace routinely the Reynolds averaged Navier-Stokes approach (RANS) by the turn of the 21st century, it appears crystal clear today that the large-eddy simulation (LES) in spite of its continuous improvement (Hanjalić and Launder (2020)) did not live up to its expectations. Indeed, its application to many industrial flows at high Reynolds and Rayleigh numbers is still out of reach and will remain so during the many years to come. Thus, in a rather pragmatic move, many efforts were progressively directed during the last two decades towards the development of hybrid methods e.g. methods able to resolve at least partially the flow unsteadiness, especially in regions where RANS finds its limit e.g. flow areas featuring massive separations and large-scale energy-containing vortical structures leading to a turbulence far from equilibrium. Along these lines, a first alternative was to combine RANS, the workhorse of the last forty years of computational fluid dynamics (CFD) and LES in a so-called hybrid RANS/LES method. There exists quite a rich variety of hybrid RANS/LES methodologies classified as zonal methods for which the zones targeted by either the RANS or the LES treatment are defined prior to the simulation and non-zonal methods where it is the model itself which is able to switch smoothly between the two modes according to some given criteria. The interested reader is referred to Chaouat (2017) for quite an exhaustive review of hybrid RANS/LES methods and to Duffal et al. (2021) as an example of recent advances in the development of a seemless hybrid temporal filtered LES. The second alternative to elaborate a hybrid method is to retain the RANS framework but to revisit the derivation of its governing equations in a way that permits the derivation of a sound unsteady RANS (URANS) model. The partially filtered Navier-Stokes (PANS) model proposed originally by Girimaji (2006) and the scale-adapted simulation approach (SAS) developed by Menter and co-authors [Menter et al. (2003), Menter and Egorov (2005), Menter and Egorov (2006)] belong to this class of models and are termed as second generation unsteady RANS (2G-URANS) models (Fröhlich and Von Terzi (2008)). The SAS approach in particular proved to be quite efficient to simulate a significant number of flow configurations (Menter (2015)) for which it was able to resolve a substantial part of the temporal fluctuations without containing an explicit mesh dependence thanks to the absence of filtering when deriving its constitutive equations.

Since the assessment of any existing model or any newly derived model has to be validated against experimental data, the main scope of the present study is to contribute to the enrichment of the SAS validation database by simulating and analyzing a turbulent flow through a tube bundles array. By addressing the additional complexity of the strong interactions between the tubes wakes, such a test is thought of as supplementing the simulations of an isolated cylinder wake with the SAS approach carried out earlier by Menter et al. (2012) and two cylinders wake interaction developed by Grioni et al. (2018) and Grioni et al. (2020). This kind of configuration is also of practical interest since it is encountered in different engineering applications such as heat exchangers for which, obviously, the accurate prediction of the heat exchange characteristics is of paramount importance. The experiments performed by Simonin and Barcouda [Simonin and Barcouda (1986b), Simonin and Barcouda (1988), Simonin and Barcouda (1986a)] and presented during the second and third ERCOFTAC-IAHR

Workshops (ERCOFTAC-IAHR-Workshop (1993), ERCOFTAC-IAHR-Workshop (1994)) have therefore been selected to assess the predictive capabilities of the SAS approach. In the following, this experiment will be generally referred to as the S&B experiment. The corresponding flow configuration is schematically represented in Figure 1. It consists of an isothermal fluid flowing across a staggered tube bundle array. The tube bundle consists of seven staggered columns of rods with a diameter $D = 21.7\,mm$. The staggered tubes were uniformly spaced in both the streamwise and the transversal directions with a separation distance of $L = 45\,mm$ in either direction. The working fluid was water flowing through the bundle with a uniform inlet velocity of $U_0 = 1.06\,m/s$ corresponding to a Reynolds number $Re = U_0 D/\nu_{water}$ of 18000. Velocity and Reynolds stresses profiles were measured along some specific cutting lines. This flow configuration was simulated by several researchers using either RANS,

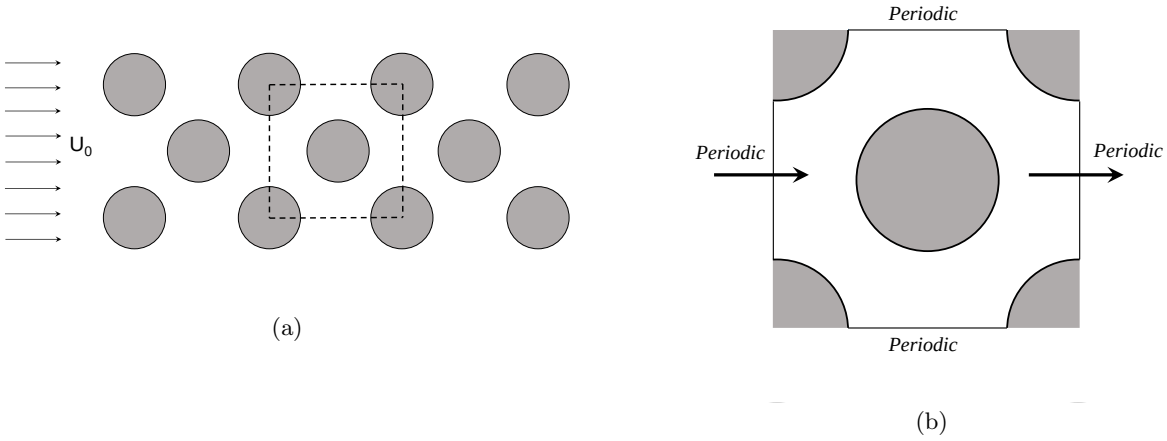


Figure 1: (a) Overview of the tube bundle array configuration experimentally investigated by Simonin and Barcouda (1986b) and Simonin and Barcouda (1988), and (b) Zoom in the zone used for comparison in the present study.

URANS, LES or Direct Numerical Simulation (DNS). RANS simulations failed to produce reliable predictions of such a flow because of the poor estimation of the turbulence kinetic energy behavior (Benhamadouche and Laurence (2003), Paul et al. (2008), Ridluan and Tokuhiro (2008a)). Results of URANS simulation using a Reynolds stress model (RSM) exhibited a better agreement with experimental data than RANS (Johnson (2008)) although some discrepancies still remained when it came to reproduce the Reynolds normal stress behavior (Ridluan and Tokuhiro (2008b)). LES seems to show the most promising results (Rollet-Miet et al. (1999), Hassan and Barsamian (2004)) although some studies comparing LES with some models with lower computational cost suggested that the difference in the predictive capabilities of these different methodologies was rather marginal (Benhamadouche and Laurence (2003), Minelli et al. (2017)). Indeed, both LES and a RSM-based URANS approach were able to provide quite satisfactory results in comparison with experiments, the former being slightly more consistent with the DNS results though (Benhamadouche and Laurence (2003)). A recent study using PANS and LES reported that both methods predicted the flow in a relatively good

and similar agreement with the experimental data although the PANS simulation was applied on a much coarser grid than LES (Minelli et al. (2017)). Not surprisingly, the results of DNS simulations (Moulinec et al. (2004)), although performed at a lower Reynolds number to limit the computational cost, proved to be also in line with the experimental data. Thus, it appears that the most appropriate method to be selected depends on the expectation of the engineer related to the accuracy of results and the computational requirements the user is prepared to expend on the problem. For the authors of the present work, the SAS approach represents a good compromise between accuracy and computational cost that makes it sufficiently attractive to justify testing it on the flow across a tube bundle.

The remaining part of this paper is organized as follows: In Section 2, the general information about the governing equations and the turbulence modeling is provided. In Section 3, all the information concerning the numerical modeling is given. In Section 4, the results obtained with the SST-SAS model for the flow in a staggered tube bundle array are presented and compared with the experimental data and other simulation results. Finally, in Section 5, the concluding remarks of this study are presented.

## 2 The continuous flow model

By ensemble averaging the continuity and the Navier-Stokes equations for a constant-density, isothermal and incompressible body force free flow, expressed in the cartesian system of coordinates $(O, x_1, x_2, x_3)$, the following set of governing equations e.g. the unsteady Reynolds averaged Navier-Stokes (URANS) system is readily obtained, namely:

$$\frac{\partial \langle u_i \rangle}{\partial x_i} = 0 \tag{1}$$

$$\frac{\partial \langle u_i \rangle}{\partial t} + \frac{\partial \langle u_i \rangle \langle u_j \rangle}{\partial x_j} = -\frac{1}{\rho}\frac{\partial \langle p \rangle}{\partial x_i} + \frac{\partial}{\partial x_j}\left[\nu\left(\frac{\partial \langle u_i \rangle}{\partial x_j} + \frac{\partial \langle u_j \rangle}{\partial x_i}\right) - \langle {u_i}' {u_j}' \rangle\right] \tag{2}$$

where for any instantaneous variable $\phi(x_i, t)$ (the pressure $p$ or the velocity components $u_i$) $\langle \phi \rangle(x_i, t)$ stands for its ensemble mean which is related to $\phi(x_i, t)$ by:

$$\phi(x_i, t) = \langle \phi \rangle(x_i, t) + \phi'(x_i, t) \tag{3}$$

where the turbulent fluctuations $\phi'(x_i, t)$ are such that $\langle \phi'(x_i, t) \rangle = 0$. The ensemble average $\langle \phi \rangle$ can be formally redecomposed into a (long) time average $\overline{\Phi}$ and a coherent e.g. non-turbulent fluctuation $\tilde{\phi}$, namely:

$$\langle \phi \rangle(x_i, t) = \overline{\Phi}(x_i) + \tilde{\phi}(x_i, t) \tag{4}$$

For a graphical illustration of the different averages and related fluctuations introduced above, the interested reader is referred to Fig. 1 and 2 in Johnson (2008). To close the above set of equations, the Reynolds stress tensor $\langle {u_i}' {u_j}' \rangle$ is expressed through a Boussinesq-like relation, namely:

$$\langle {u_i}' {u_j}' \rangle = -\nu_t \left(\frac{\partial \langle u_i \rangle}{\partial x_j} + \frac{\partial \langle u_j \rangle}{\partial x_i}\right) + \frac{2}{3} k \delta_{ij} \tag{5}$$

where the turbulent eddy viscosity $\nu_t$ and the turbulence kinetic energy $k$ are calculated thanks to the recourse to the SST-SAS turbulence model.

## 2.1 SST-SAS turbulence model

The SST-SAS turbulence model was developed by Menter and co-authors [Menter and Egorov (2005), Egorov and Menter (2008), Menter and Egorov (2010) (see also Davidson (2006))] to adapt the SAS approach (Menter et al. (2003)) to the $k-\omega$ SST eddy-viscosity RANS model (Menter (1994)). It is based on the reformulation of the exact transport equation of the turbulence length scale originally derived by Rotta (1972). The resulting SST-SAS model distinguishes itself from the original SST model by the addition of a SAS related source term into the equation of the turbulence frequency $\omega$, leaving unchanged the equation for the turbulence kinetic energy $k$. The paper referred to in the Ansys-Fluent documentation for the description of the implemented version of the SST-SAS model in the 15.0 release of the software is Menter and Egorov (2010) although some minors deviations were noted between that paper and the documentation. By concatenating the previously mentioned sources of information regarding the description of the SST-SAS, the corresponding set of equations reads as:

$$\frac{\partial k}{\partial t} + \langle u_j \rangle \frac{\partial k}{\partial x_j} = P_k - \beta^* k\omega + \frac{\partial}{\partial x_j}\left[\Gamma_k \frac{\partial k}{\partial x_j}\right] \tag{6}$$

$$\frac{\partial \omega}{\partial t} + \langle u_j \rangle \frac{\partial \omega}{\partial x_j} = \frac{\gamma}{\mu_t} P_k - \beta \omega^2 + \frac{\partial}{\partial x_j}\left[\Gamma_\omega \frac{\partial \omega}{\partial x_j}\right] + (1 - F_1)\frac{2}{\sigma_{\omega,2}}\frac{1}{\omega}\frac{\partial k}{\partial x_j}\frac{\partial \omega}{\partial x_j} + Q_{SAS} \tag{7}$$

where $P_k = \nu_t S^2$ with $S = \sqrt{2 S_{ij} S_{ij}}$ and $S_{ij} = \frac{1}{2}\left(\frac{\partial \langle u_i \rangle}{\partial x_j} + \frac{\partial \langle u_j \rangle}{\partial x_i}\right)$. The turbulent viscosity is calculated as:

$$\nu_t = \frac{k}{\omega} \frac{1}{max\left[1/\alpha^*; SF_2/a_1\omega\right]} \tag{8}$$

where the low Reynolds number correction related coefficient $\alpha^*$ is defined as:

$$\alpha^* = \left(\frac{{\alpha^*}_0 + Re_t/R_k}{1 + Re_t/R_k}\right) \tag{9}$$

with $Re_t = k/(\nu\omega)$, $R_k = 6$, $a_1 = 0.31$ and ${\alpha^*}_0 = 0.024$. The so-called blending function $F_2$ was designed so as to vary smoothly between 1 in the vicinity of solid walls (full $k-\omega$ behavior) to 0 far from the walls (full $k-\epsilon$ behavior), namely:

$$F_2 = tanh({\Phi_2}^2) \text{ with } \Phi_2 = max\left[2\frac{\sqrt{k}}{0.09\omega y}; \frac{500\nu}{y^2\omega}\right] \tag{10}$$

The constant $\beta^*$ is taken equal to 0.09. The turbulent diffusivities are expressed as:

$$\Gamma_k = \left(\nu + \frac{\nu_t}{\sigma_k}\right) \text{ and } \Gamma_\omega = \left(\nu + \frac{\nu_t}{\sigma_\omega}\right) \tag{11}$$

with:

$$\sigma_k = \frac{1}{F_1/\sigma_{k,1} + (1 - F_1/)\sigma_{k,2}} \text{ and } \sigma_\omega = \frac{1}{F_1/\sigma_{\omega,1} + (1 - F_1/)\sigma_{\omega,2}} \tag{12}$$

where the indices $_{,1}$ and $_{,2}$ stand for the constant values for the $k-\omega$ model and the $k-\varepsilon$ model, respectively, and $y$ denotes the distance to the closest wall (if any). The values of the constants are

chosen as $\sigma_{k,1} = 1.176$, $\sigma_{k,2} = 1.000$, $\sigma_{\omega,1} = 2.000$ and $\sigma_{\omega,2} = 1.168$. The blending function $F_1$ is defined as:

$$F_1 = tanh({\Phi_1}^4) \text{ with } \Phi_1 = min\left[max\left[2\frac{\sqrt{k}}{0.09\omega y}; \frac{500\nu}{y^2\omega}\right]; \frac{4\rho k}{\sigma_{\omega,2} D_\omega^+ y^2}\right] \tag{13}$$

where $D_\omega^+$ stands for the positive part of the cross-diffusion terms, namely:

$$D_\omega^+ = max\left[\frac{2}{\sigma_{\omega,2}}\frac{1}{\omega}\frac{\partial k}{\partial x_j}\frac{\partial \omega}{\partial x_j}; 10^{-10}\right] \tag{14}$$

Leaving out the compressibility corrections which are not relevant for the constant-density flow considered in the present study, the terms $\gamma$ and $\beta$ in Eq. (7) are calculated as:

$$\gamma = \frac{\alpha_\infty}{\alpha^*}\left(\frac{{\alpha^*}_0 + Re_t/R_\omega}{1 + Re_t/R_\omega}\right) \text{ with } \alpha_\infty = F_1\alpha_{\infty,1} + (1-F_1)\alpha_{\infty,2};\ R_\omega = 2.95 \tag{15}$$

$$\beta = F_1\beta_{i,1} + (1-F_1)\beta_{i,2} \tag{16}$$

where

$$\alpha_{\infty,1} = \frac{\beta_{i,1}}{\beta^*} - \frac{\kappa^2}{\sigma_{\omega,1}\sqrt{{\beta^*}_\infty}} \text{ and } \alpha_{\infty,2} = \frac{\beta_{i,2}}{\beta^*} - \frac{\kappa^2}{\sigma_{\omega,2}\sqrt{{\beta^*}_\infty}} \tag{17}$$

with ${\beta^*}_\infty = \beta^* = 0.09$, $\beta_{i,1} = 0.0750$, $\beta_{i,2} = 0.0828$ and where $\kappa = 0.41$ is the von Kármán constant. The additional source term ($Q_{SAS}$) is given in Egorov and Menter (2008) as:

$$Q_{SAS} = max\left[\xi_2\kappa S^2\left(\frac{L}{L_{vk}}\right)^2 - C_{SAS}\frac{2k}{\sigma_\Phi}max\left(\frac{1}{\omega^2}\frac{\partial\omega}{\partial x_j}\frac{\partial\omega}{\partial x_j}; \frac{1}{k^2}\frac{\partial k}{\partial x_j}\frac{\partial k}{\partial x_j}\right), 0\right] \tag{18}$$

where the SAS model parameters are given by $\xi_2 = 3.51$, $\sigma_\Phi = 2/3$ and $C_{SAS} = 2$. The turbulence length scale ($L$) is calculated as:

$$L = \frac{\sqrt{k}}{{c_\mu}^{0.25}\omega} \tag{19}$$

Central to the SAS approach, the von Karman length-scale $L_{vk}$ acts as a sensor to detect the flow unsteadiness susceptibility in the resolved velocity field, it is defined as:

$$L_{vk} = \kappa\sqrt{\left|\frac{\frac{\partial\langle u_i\rangle}{\partial x_j}\frac{\partial\langle u_j\rangle}{\partial x_i}}{\frac{\partial^2\langle u_i\rangle}{\partial x_j^2}\frac{\partial^2\langle u_j\rangle}{\partial x_i^2}}\right|} \tag{20}$$

The treatment of the boundary conditions for $k$ and $\omega$ at solid walls is designed so as to switch automatically from a viscous sublayer formulation ($k = 0$ and $\omega = 6\nu/(0.075y^2)$ at the wall) to a wall function approach ($\partial k/\partial n = 0$ and $\omega = u_\tau^{log}/(0.3\kappa y)$ at the boundary, where $n$ stands for the direction normal to the wall and $u_\tau^{log} = \langle u\rangle\kappa/\left[ln(y^+) + \kappa C\right]$), depending on the near-wall grid refinement.

# 3 Method of solution, choice of the simulations parameters and data post-processing

## 3.1 Method of solution

The numerical solver utilised in this research is the commercial CFD code FLUENT, which is part of the ANSYS 15.0.7 software suite. The FLUENT code uses the finite volume cell-centered method to solve in a segregated way the governing equations (1), (2), (6) and (7). These equations are spatially discretized on three-dimensional structured O-type grids, an example of which is shown in Figure 2. The convection terms are discretized using a bounded central differencing scheme, while the pressure

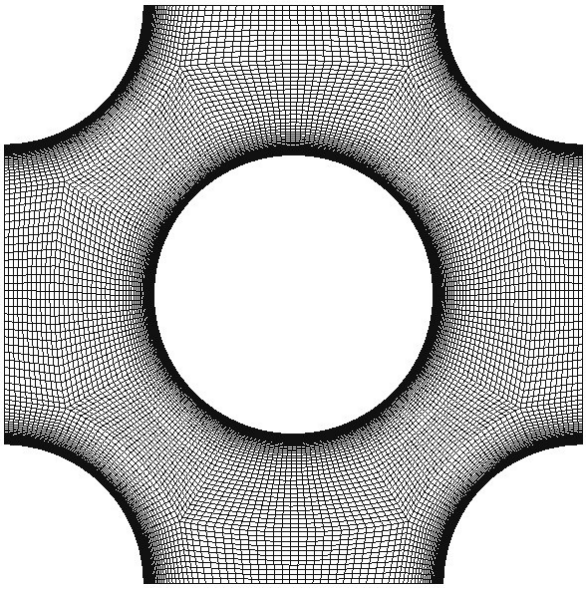

Figure 2: Example of a structured O-type mesh used in the present study (2D cutting view of mesh $\mathcal{M}_2$).

and the turbulent quantities ($k$ and $\omega$) are evaluated with a second-order scheme. The equations are further discretized in time by using a bounded second-order implicit scheme. The SIMPLE (Semi-Implicit Method for Pressure Linked Equations) algorithm (Patankar and Spalding (1972)) is used for handling the coupling between the pressure and the velocity fields.

## 3.2 Choice of the simulation parameters

### 3.2.1 Residual tolerance

A study of the sensitivity of the results to the targeted maximum level of the residuals of the equations was carried out. In addition to the default value of $10^{-3}$, two more stringent values were considered e.g. $10^{-4}$ and $10^{-5}$. The marginal sensitivity of the results to the change of the maximum level of residuals is illustrated in Figure 3. The streamwise mean velocity (U_velocity) profile at position $x = 0mm$ is presented as well as the turbulence kinetic energy ($k$) spectrum plotted against the

Strouhal number $St = fD/U_{bulk}$, where $f$ is the peak frequency of the velocity signal monitored in the wake of the central cylinder at point $[0.77D, 0D, 1D]$. As can be inferred from the analysis of both plots, the default choice of $10^{-3}$ is perfectly adequate and was therefore retained for all the subsequent simulations for which 3 to 10 inner SIMPLE iterations per time step were found to be sufficient to resolve the pressure-velocity coupling.

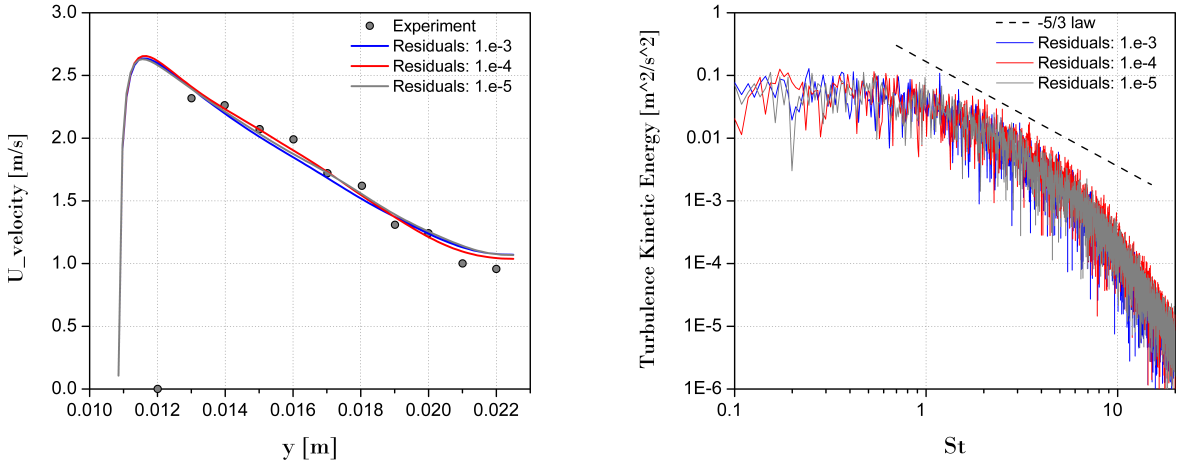


(a) (b)

Figure 3: Sensitivity to the choice of the residuals' tolerance: (a) Profile of the streamwise mean velocity at $x = 0\ mm$ and (b) Turbulence energy spectrum at point $[0.77D, 0D, 1D]$ against the Strouhal number $St = fD/U_{bulk}$.

### 3.2.2 Mesh and time step sensitivity analysis

The effect of the mesh size and time resolution are evaluated by comparing the mean drag coefficient $\overline{\langle C_D \rangle} = \frac{\overline{\langle F_D \rangle}}{0.5\rho {U_{bulk}}^2 A}$ and lift coefficient $\overline{\langle C_L \rangle} = \frac{\overline{\langle F_L \rangle}}{0.5\rho {U_{bulk}}^2 A}$ as well as the peak value of the Strouhal number observed on the spectrum of the time evolution of the ensemble averaged lift coefficient $\langle C_L \rangle$. $F_D$ and $F_L$ are the instantaneous unsteady drag and lift forces exerted on the central tube of projected area $A$, respectively. The adopted meshing strategy produced multi-block O-type structured meshes featuring a refinement in the vicinity of the tubes walls. Any wall adjacent cell (AC) size was chosen so as to ensure that $({y^+}_{AC} = y_{AC}\overline{\langle u_\tau \rangle}/\nu < 1$ wall unit) where $\overline{\langle u_\tau \rangle}$ denotes the time average of the local ensemble averaged friction velocity and $y_{AC}$ stands for the normal distance between the cell center and the wall. The three tested meshes were denoted by $\mathcal{M}_\mathbf{1}$ (coarse mesh, 420000 cells), $\mathcal{M}_\mathbf{2}$ (medium mesh, 850000 cells) and $\mathcal{M}_\mathbf{3}$ (fine mesh, 1700000 cells), respectively. For the simulations carried out for these three different meshes, the dimensionless time step was kept constant and equal to $\Delta t = 0.0082D/U_{bulk}$ corresponding to a maximum CFL number below 2 for mesh $\mathcal{M}_\mathbf{2}$.

In parallel, a sensitivity analysis of the results to the time step value using the medium mesh $\mathcal{M}_\mathbf{2}$ was carried out. Three different dimensionless time steps were considered namely $\Delta t U_{bulk}/D = 0.0164$, 0.0082 and 0.0041, respectively. For mesh $\mathcal{M}_\mathbf{2}$, the latter time step value ensured that CFL$<$ 1 over

the entire computational domain. Table 1 regroups the various results that were obtained for this mesh and time step sensitivity analysis.

Table 1: Sensitivity to the mesh size and the time step values.

| Cases | Number of cells (millions) | $\Delta t U_{bulk}/D$ | $\overline{\langle C_D \rangle}$ | $St_{\langle C_L \rangle}$ |
|---|---|---|---|---|
| *Mesh size* | | | | |
| Coarse ($\mathcal{M}_\mathbf{1}$) | $\sim 0.42$ | 0.0082 | 0.49 | 0.40 |
| Medium ($\mathcal{M}_\mathbf{2}$) | $\sim 0.85$ | 0.0082 | 0.51 | 0.41 |
| Fine ($\mathcal{M}_\mathbf{3}$) | $\sim 1.7$ | 0.0082 | 0.51 | 0.41 |
| *Time resolution* | | | | |
| Large | $\sim 0.85$ | 0.0164 | 0.52 | 0.43 |
| Intermediate | $\sim 0.85$ | 0.0082 | 0.51 | 0.41 |
| Small | $\sim 0.85$ | 0.0041 | 0.50 | 0.41 |

On the one hand, it can be seen that the difference between the results obtained for meshes $\mathcal{M}_\mathbf{2}$ and $\mathcal{M}_\mathbf{3}$ are similar, while those obtained with mesh $\mathcal{M}_\mathbf{1}$ are noticeably different. On the other hand, the results from the time step sensitivity analysis show an evident convergence of both $\overline{\langle C_D \rangle}$ and $St_{\langle C_L \rangle}$, indicating that the choice of the intermediate time step represents a good compromise. As a consequence, it was decided to perform all the simulations using mesh $\mathcal{M}_\mathbf{2}$ with the intermediate time step value. This three-dimensional mesh $\mathcal{M}_\mathbf{2}$ was generated by extruding in the $z$-direction over a distance of $2D$ the two-dimensional mesh displayed in Figure 2 with 42 cells equidistantly located in that direction which is the lowest limit recommended in Menter et al. (2003).

## 3.3 Data post-processing

### 3.3.1 Computation of the time averages

The determination of the proper minimum duration over which the time averaging must be carried out was guided by a preliminary analysis of the sensitivity of the averages to the time interval of integration.

Four different durations of data recording (corresponding to four different numbers of periods at frequency $f_{\langle C_L \rangle} = St_{\langle C_L \rangle} U_{bulk}/D$ covered by the time integration) were considered for calculating the time average of the ensemble averaged velocity components $\overline{\langle U \rangle}$ and $\overline{\langle V \rangle}$ at position $x = 0\,mm$. It can be inferred from the results displayed in Figure 4 that an integration over a time interval corresponding to at least 48 cycles at frequency $f_{\langle C_L \rangle}$ is sufficient to ensure a fair convergence of the average estimators. Accordingly, the employed procedure was the following: the transient simulations were first run until the flow reached a permanent regime of unsteadiness, i.e. once a regular periodicity pattern was established. Then, the simulation was pursued during a time duration corresponding to about 50 vortex-shedding cycles in order to calculate reliable time averaged data.

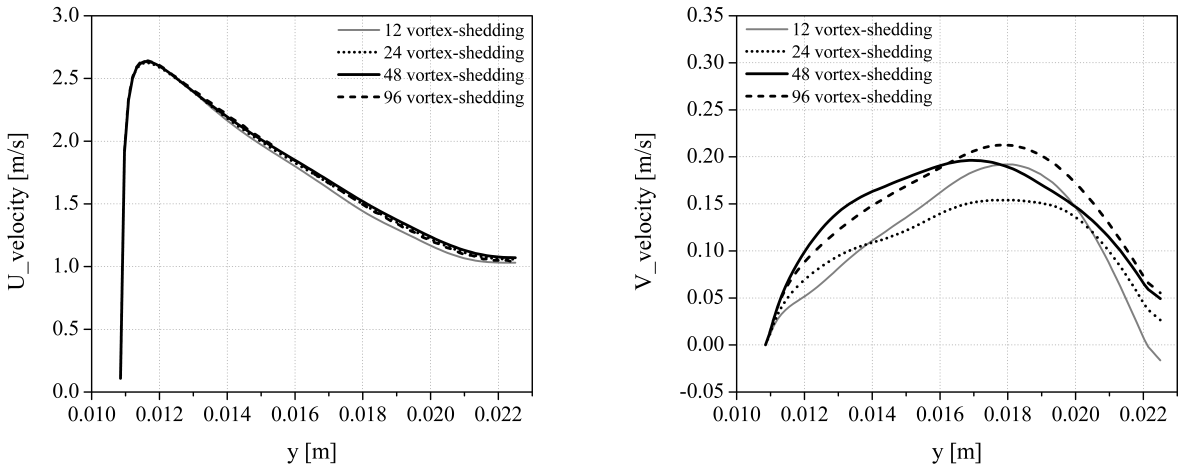


(a) (b)

Figure 4: Sensitivity of the time average of the ensemble averaged velocity at $x = 0\ mm$ to the number of cycles over which the time average is performed: a) streamwise component and b) normal component.

### 3.3.2 Computation of the total Reynolds stresses

As pointed out by Johnson (2008), the experiments such as the S&B experiment [Simonin and Barcouda (1986a), Simonin and Barcouda (1986b), Simonin and Barcouda (1988)] provide the (long) time average of the experimental data. As such, they yield in particular the total velocity correlations noted $\overline{u_i'' u_j''}$ which sum up the contribution of the coherent fluctuations and that of turbulence, namely:

$$\overline{u_i'' u_j''} = \overline{\langle u_i' u_j' \rangle} + \overline{\tilde{u_i} \tilde{u_j}} \tag{21}$$

So, to confront the experimental data with those resulting from the simulations, it is necessary to post-process the numerical results to provide the relevant numerical counterpart of the experimental data. The first term on the right hand side in Eq. 21 is provided by the time average of the modeled Reynolds stress and the second term represents the contribution of the coherent fluctuations to the total stress. This term can be calculated directly from the resolved velocity fluctuations which can be expressed as:

$$\overline{\tilde{u_i} \tilde{u_j}} = \overline{\left(\langle u_i \rangle - \overline{\mathbf{u}}_i\right)\left(\langle u_j \rangle - \overline{\mathbf{u}}_j\right)} = \overline{\langle u_i \rangle \langle u_j \rangle} - \overline{\langle u_i \rangle \overline{\mathbf{u}}_j} - \overline{\overline{\mathbf{u}}_i \langle u_j \rangle} + \overline{\overline{\mathbf{u}}_i\, \overline{\mathbf{u}}_j} \tag{22}$$

considering that $\overline{\mathbf{u}}_i$ and $\overline{\mathbf{u}}_j$ are constant and that the time average of the ensemble average velocity is equal to the time average velocity, the last three terms can be added to obtain that:

$$\overline{\tilde{u_i} \tilde{u_j}} = \overline{\langle u_i \rangle \langle u_j \rangle} - \overline{\mathbf{u}}_i\, \overline{\mathbf{u}}_j \tag{23}$$

Thus, the total Reynold stress average is finally obtained as

$$\overline{u_i'' u_j''} = \overline{-\frac{\mu_t}{\rho}\left(\frac{\partial\langle u_i\rangle}{\partial x_j} + \frac{\partial\langle u_j\rangle}{\partial x_i}\right) + \frac{2}{3}k\delta_{ij}} + \overline{\langle u_i\rangle\langle u_j\rangle} - \overline{\mathbf{u}}_i\,\overline{\mathbf{u}}_j \tag{24}$$

This expression is implemented in FLUENT through a 'user-defined function' (UDF).

# 4 Results

## 4.1 Numerical set-up

All the geometrical parameters, flow conditions and measurements of the S&B experiment provided by the ERCOFTAC database (Simonin and Barcouda (1986a)) were used to set-up the present computations. It is worth stressing though that the database does not contain information regarding the bias and precision errors (neither systematic nor random) of the measurements. So in the subsequent figures neither error bars nor estimates of uncertainties will be provided.

The measurements were reported to be carried out in a region (from the fourth row onwards) where the flow featured a full development characterized by the periodicity of the (long) time averaged velocity field. Assuming that the periodicity holds also for the ensemble averaged velocity field, the computational domain was restricted to an elementary unit cell as shown in Figure 5. Periodic boundary conditions were applied to the velocity field in the transversal $Oy$, and spanwise $Oz$ directions. In order to respect the mean experimental mass flow rate e.g. $\dot{Q} = \rho_{water} U_{bulk} S$, the periodicity in the streamwise direction $Ox$ direction was combined with an imposed pressure gradient between the section at $x = -L/2 = -22.50\ mm$ and that at $x = +L/2 = +22.50\ mm$. $S = 1.011\,10^{-3} m^2$ corresponds to the surface of the flow passage section (in the oyz plane) at $x = -L/2 = -22.50\ mm$ where $U_{bulk}$ has to be determined. In absence of measurements at $x = -22.50\ mm$, the profile of the streamwise component of the velocity at $x = 0\ mm$ (featuring the same flow passage section as at $x = -22.50\ mm$ ) was integrated to finally obtain the value $U_{bulk} = 1.780\,m/s$ which is in excellent agreement with the value of $1.752\,m/s$ used by Johnson (2008). It is worth noticing that in order to be as accurate as possible, the missing experimental data near the tube wall were supplemented by the results provided by the DNS of Moulinec et al. (2004). Thus, with $\rho_{water} = 998.2\,kg/m^3$, the targeted mass flow rate amounted to $\dot{Q} = 1.8\,kg/s$.

In the ERCOFTAC database (Simonin and Barcouda (1986a)), experimental results are provided at various locations for the $Ox$ and $Oy$-components of the (long) time averaged velocity as well as for the related Reynolds stresses. In the present study, three measurements lines were chosen for comparison with the numerical results, namely $x = 0$ and $11\,mm$ and $y = 0\,mm$ (see Figure 5). This choice permits to cover regions where the flow is known to feature specific characteristics such as flow reversal or strong accelerations.

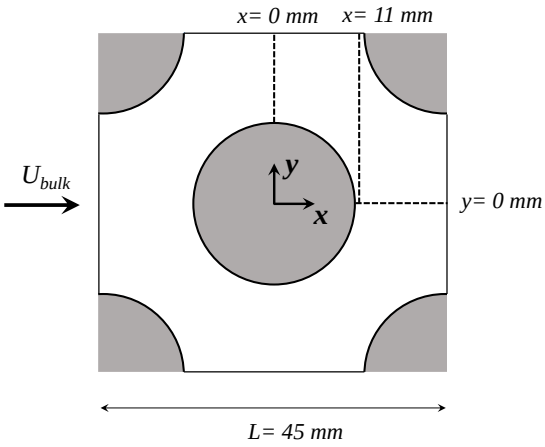


Figure 5: Computational domain (in white) and boundary conditions. Zoom in the zone experimentally investigated with indications of the lines of measurements used for comparison in the present study.

## 4.2 Illustration of the flow unsteadiness

The flow unsteadiness is first exemplified by presenting the time evolution of two components of the ensemble average velocity at point $(-L/2,-0.32D,\ 1D)$. As can been seen in Figure 6 (top), these 1.4 s-long time signals exhibit large amplitude fluctuations and are in that respect very similar to those shown by Minelli et al. (2017) at the very same position. The corresponding power spectrum density of these signals shown in Figure 6 (bottom) features a distinctive peak at frequency $f_{peak} = 33.86Hz$ that corresponds to a Strouhal number of about 0.41, a value similar to that obtained for the ensemble averaged lift coefficient. The large-scale flow unsteadiness can be qualitatively illustrated by looking at time series of successive snapshots taken in the Oxy plane located at $z = 1D$ like those presented in Figure 7 (for the velocity streamwise component) and in Figure 8 (for the z-vorticity component). The snapshots are equally spaced in time and chosen such that the time interval between the first and the last one corresponds to $1/f_{peak}$ e.g. one period of the Fourier component at frequency $f_{peak}$. The large scale flow unsteadiness manifests itself by a succession of low-speed and high speed fluid pockets that alternatively populate the upper and lower parts of the flow domain. Such a behavior was already reported by Minelli et al. (2017) when analyzing their PANS and LES based simulations.

The time evolution of the field of the z-vorticity component reveals that such pockets are accompanied by the presence of much smaller structures mainly created in the shear layers close to the tubes' walls and then swept out of the computational domain. As expected, the continuous shedding of vortical structures in the central cylinder wake leads to a significant unsteadiness of the forces exerted by the fluid on the cylinder walls. As can be seen in Figure 9, this is the ensemble averaged lift coefficient (whose long time average is zero) which exhibits a significantly larger amplitude of fluctuations in time when compared to the drag coefficient time evolution.

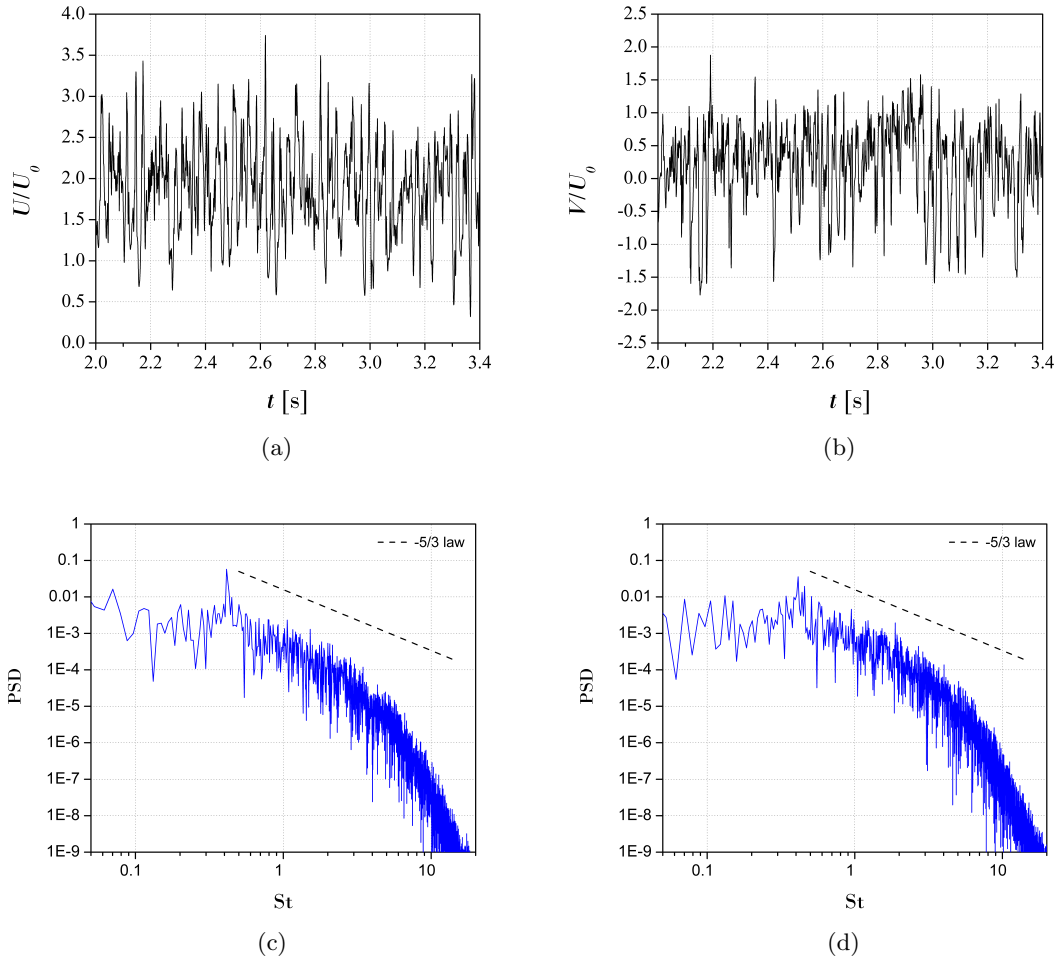


Figure 6: Illustration of the ensemble averaged velocity field unsteadiness at point $(-L/2, 0.32D, 1D)$: Top - Time history of the ensemble averaged velocity: (a) Streamwise component and (b) Normal component. Bottom - Corresponding signals power spectrum density (PSD) vs Strouhal number: (c) Streamwise component and (d) Normal component.

As far as the present SST-SAS methodology is concerned and considering the large amplitude of the flow unsteadiness, it is natural to question the respective contribution of the modeled and resolved part of the motion to the total Reynolds stresses which sum up both contributions.

As it is illustrated in Figure 10 for the profiles of the total longitudinal and normal stresses at $x = 11\,mm$, the contribution of the resolved motion to the total stress can represent up to more than 95 % and remains significantly higher than what is observed for its URANS-RSM counterpart reported by Johnson (2008) and Benhamadouche and Laurence (2003) whose evolution is also included for comparison. Such a high level of the relative contribution of the resolved motion to the total Reynolds stresses is also observed over the whole domain except in the vicinity of the tubes' wall where, as expected, the damping of the velocity unsteadiness by the viscous forces becomes predominant.

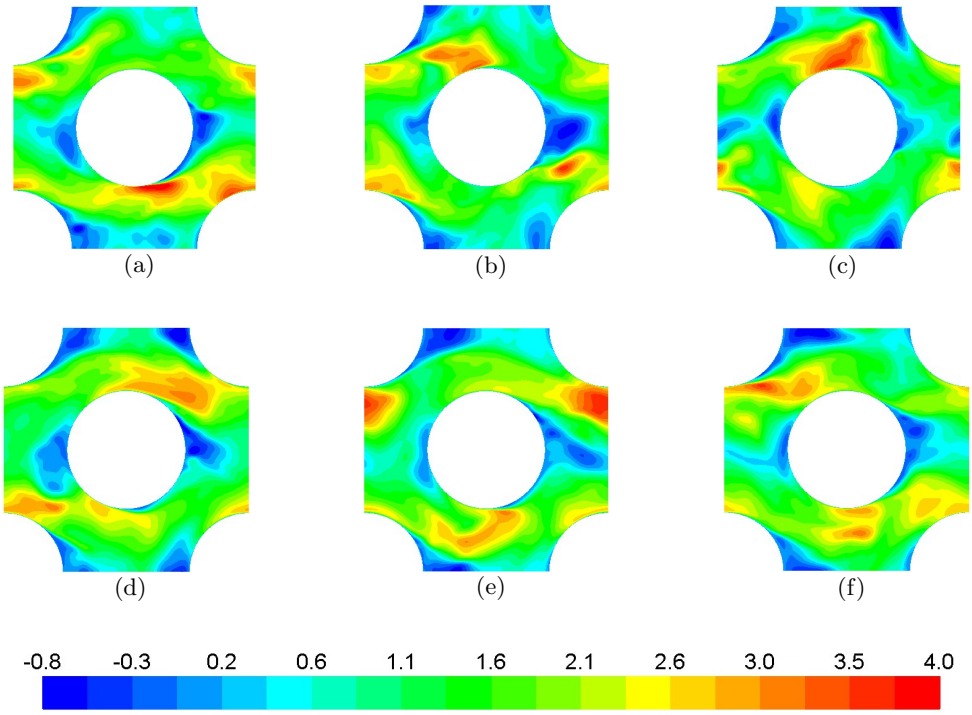


Figure 7: Time series of the 2-D field of the streamwise component of the ensemble averaged velocity in the Oxy plane located at $z = 1D$ (Color scale unit in $[m/s]$). The time interval between two consecutive snapshots is of 0.006s.

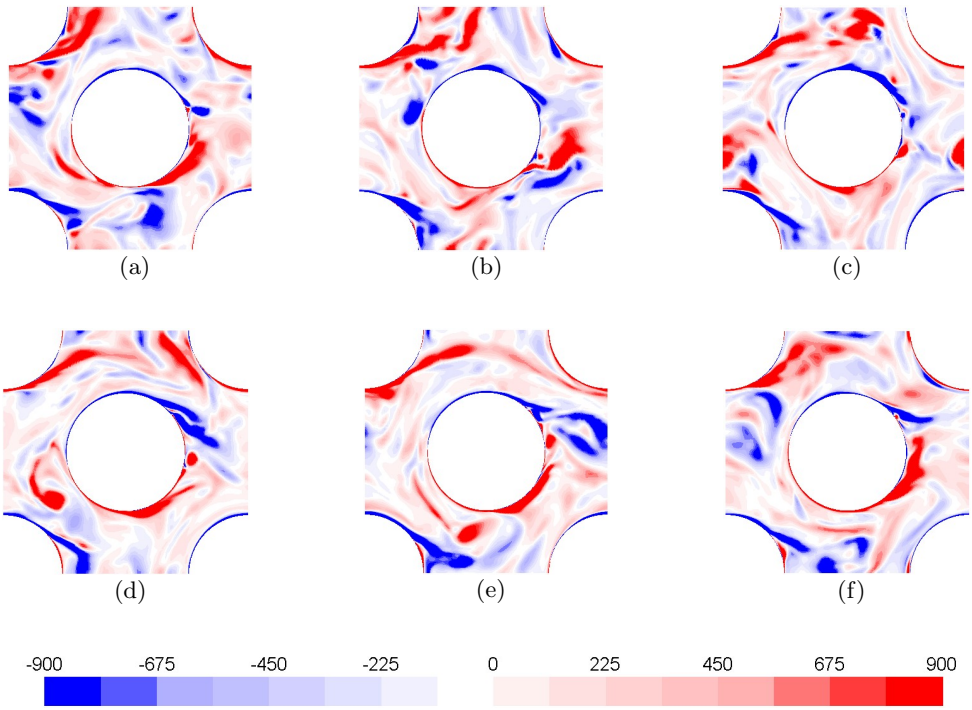


Figure 8: Time series of the 2-D field of the z-vorticity component in the Oxy plane located at $z = 1D$ (Color scale unit in $[s^{-1}]$). The time interval between two consecutive snapshots is of 0.006s.

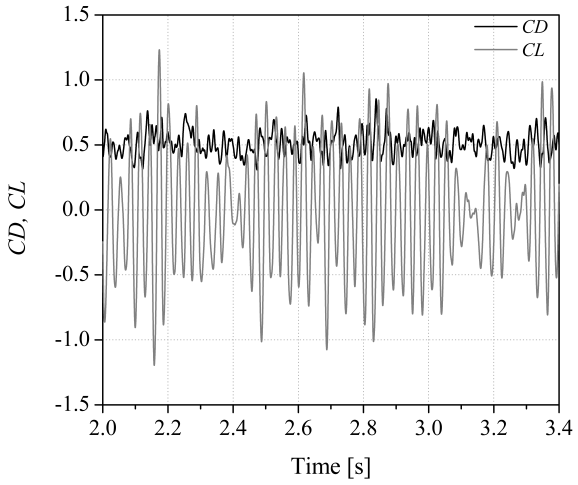


Figure 9: Time history of the ensemble averaged drag $\langle C_D \rangle$ and lift $\langle C_L \rangle$ coefficients of the aerodynamical forces exerted over the central tube.

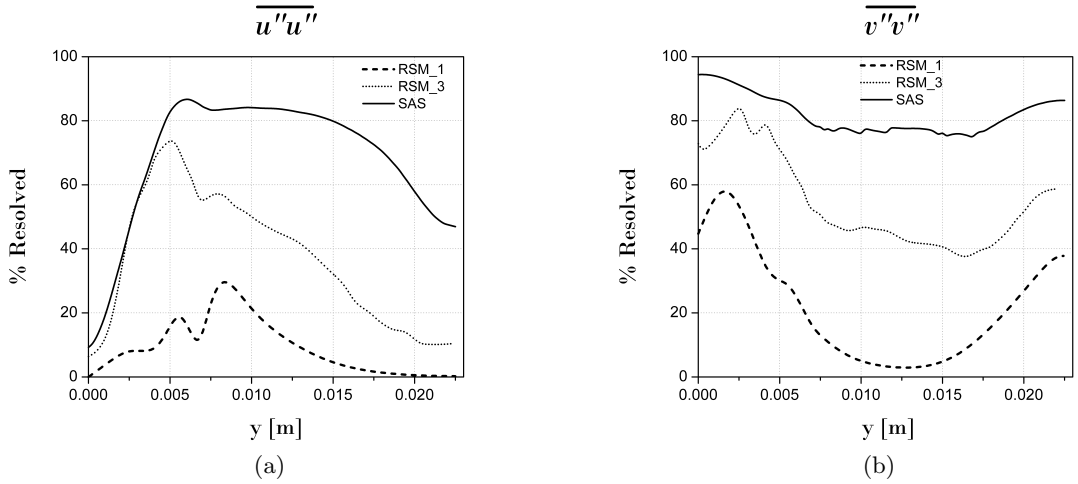


Figure 10: Relative Contribution of the resolved part of the motion to the total Reynolds stresses at $x = 11\,mm$: (a) longitudinal stress and (b) normal stress. RSM_1 results corresponds to Johnson (2008) and RSM_3 corresponds to Benhamadouche and Laurence (2003).

## 4.3 Model performance assessment

Beyond the sole comparison with the results from the S&B experiment, the present results are also confronted with the simulations results taken from the literature: The LES and PANS results by Minelli et al. (2017) and the transient RSM by Johnson (2008) (labelled RSM_1) and by Ridluan and Tokuhiro (2008b) (labelled RSM_2). The assessment of the predictive capability of the present SST-SAS based simulations will be twofold: first a qualitative evaluation is carried out as the result of the visual inspection of the variables profiles at the selected measurements stations, second, an objective criterion is defined so that marks can be calculated and summed-up over all the profiles and

variables. The resulting evaluation is qualified as being "objective" as it is fairly independent of any bias that may be brought about by the simple visual inspection.

### 4.3.1 Qualitative assessment

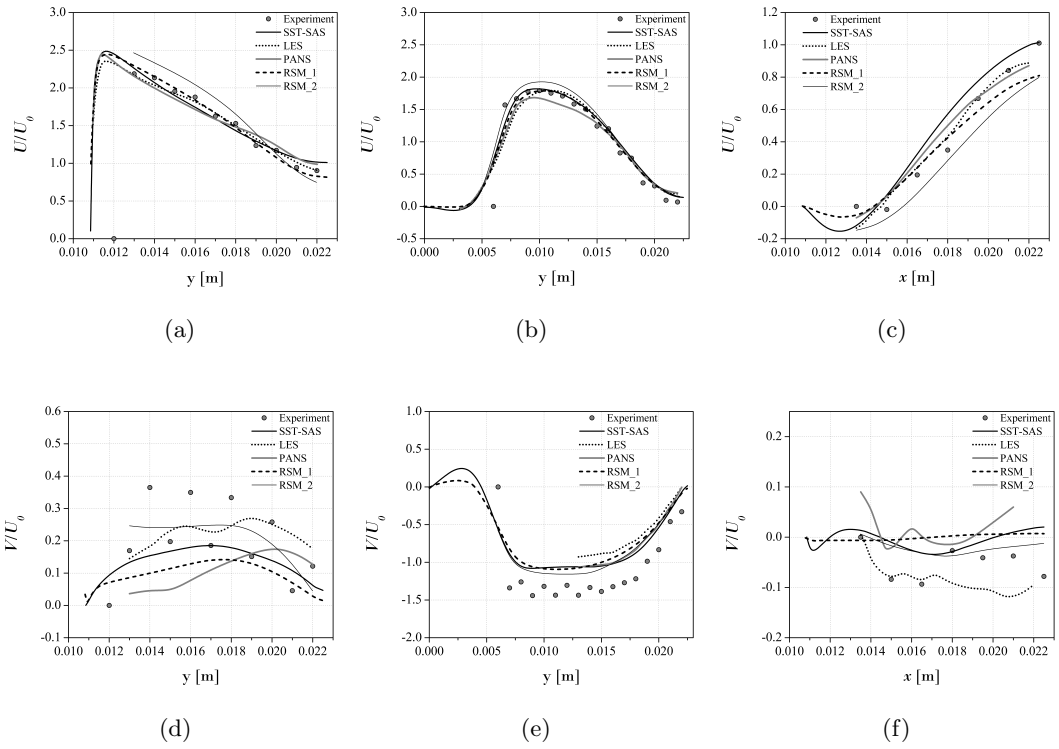


Figure 11: Profiles of the time average of the ensemble averaged velocity at $x = 0\ mm$ (left column), $x = 11\ mm$ (middle column) and $y = 0\ mm$ (right column). Top row: streamwise component. Bottom row: normal component.

The profiles of the time average of the ensemble averaged streamwise and normal components of the velocity along with the profiles of three components of the total Reynolds stress tensor are presented in Figure 11 and Figure 12, respectively. The time average was done over a 1.4 s-long period of time starting at $t = 2.0\ s$. The velocity components are normalized by the inlet velocity $U_0$, while the Reynolds stresses components are normalized by $U_0^2$.

**Mean velocity** The results obtained with the SST-SAS turbulence prove to be quite satisfactory when compared to their experimental counterpart. Indeed, the profiles of the velocity streamwise component $U$ are very well predicted by the SST-SAS calculations for the three positions, with a specific mention for the profiles at $x = 0\ mm$ (Figure 11-(a)) and at $x = 11\ mm$ (Figure 11-(b)). The profile at $y = 0\ mm$ (Figure 11-(c)) is characterised by a correct overall shape but the maximum of the flow reversal predicted by the SST-SAS simulations appears to be shifted slightly closer to the central cylinder than what was observed experimentally. Globally, all the models perform almost equally well

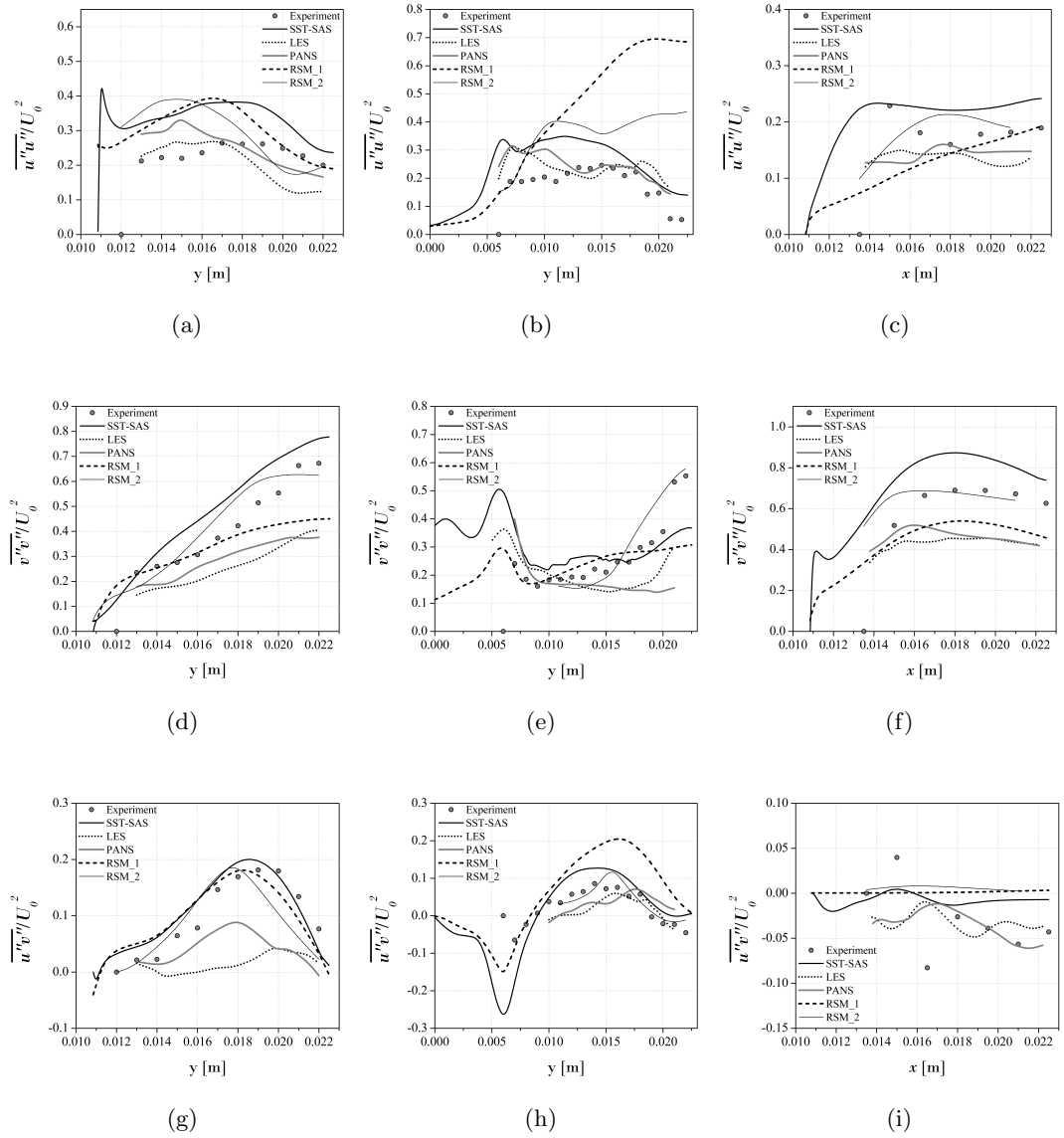


Figure 12: Profiles of the total Reynolds stresses $x = 0\ mm$ (left column), $x = 11\ mm$ (middle column) and $y = 0\ mm$ (right column). Top row : longitudinal stress. Middle row: normal stress. Bottom row: shear stress.

although the results of Ridluan and Tokuhiro (2008b) (e.g. RSM_2) are marginally less accurate. The prediction of the normal component profiles with SST-SAS is not as good as what was obtained for the longitudinal component, especially at $x = 0\ mm$ (Figure 11-(d)) and at $y = 0\ mm$ (Figure 11-(f)). Actually, none of the models was able to reproduce the experimental data with a good precision. But as recalled by Johnson (2008) though, the experimental profile of the normal velocity component at $x = 0\ mm$ concatenates measurements from points symmetrically located (with respect to the $Oy$ axis) above and below the central tube. Thus, the unexpected dispersion of the experimental values might be the signature of a part of the uncertainty in the measurements at that very location. All the models provide a fairly better agreement at the two other stations, with a particular mention for

the profiles at $x = 11\ mm$. At $y = 0\ mm$, the expected symmetry of the time average of the ensemble averaged central tube wake implies that the normal component of the velocity should remain equal to zero along the profile. This condition is clearly neither fulfilled by the experimental data nor by the LES and PANS results. On the contrary, the RSM results by Johnson (2008) (RSM_1) and to a lesser extent the present SST-SAS simulations are in line with the expected nullity of that normal velocity component.

**Total Reynold stresses** The quality of the prediction of the total Reynolds stresses profiles by the SST-SAS model could be qualified as fair and homogeneous, featuring no large discrepancy with experimental data unlike what is observed for some other simulations results. For the normal stress, $\overline{u''u''}$ (Figure 12-(a) to (c)), the SST-SAS results overestimate the experimental data but predict correctly the evolution of the experimental profiles from one position to the other. In contrast, the PANS and LES results prove to be more accurate. Concerning the normal stress $\overline{v''v''}$ at $x = 0\ mm$ (Figure 12-(d)), the SST-SAS results agree fairly well with the experimental data but this time the results of LES and PANS are clearly not as accurate while RSM_2 (the results of Ridluan and Tokuhiro (2008b)) proves to be in good agreement. At $x = 11\ mm$ (Figure 12-(e)), the SST-SAS model performs quite well while the best fit over most of the profile is achieved by RSM_1 (Johnson (2008)). For $y = 0\ mm$ (Figure 12-(f)), the RSM_2 results are quite accurate whereas the SST-SAS are above the experimental results. The LES and PANS significantly underestimate the experimental data. Finally, the profiles of the shear Reynolds stress ($\overline{u''v''}$) are presented in Figure 12-(g) to (i). At $x = 0\ mm$, the SST-SAS results along with those of RSM_1 are in good agreement with the experiments whereas the peak value appears to be largely underestimated by the PANS results and is even not clearly visible in the LES profile. At position $x = 11\ mm$, the agreement of the SST-SAS profile with its experimental counterpart is quite satisfactory over a large part of the $y$-range, but a significant difference is observed for $y \leq 6\ mm$, where the deep dive observed in the simulations is absent from the experimental data. At $y = 0\ mm$ (Figure 12-(i)), the symmetry of the flow in the wake behind the central tube would require $\overline{u''v''}$ to be zero, a criterion met by the RSM_1 results and not to badly by the SST-SAS and RSM_2 ones, in return the PANS, LES and the experimental data deviate significantly from the expected zero value of the shear stress.

### 4.3.2 Quantitative assessment

The results from the qualitative inspection of the profiles presented in the preceding section clearly illustrate the difficulty of ranking the different simulation approaches on the sole basis of the recourse to qualifications such as “underestimate” or “quite good” or “deviate significantly”. To overcome the relativity of such “judgments”, a quantitative assessment is definitely needed. To that end, for each model and at each measurements station and for each variable, a model mark was calculated from the

L2 norm of the difference between the model results and the experiments, namely:

$$Error^{\Phi}_{model} = \sum_{i=1}^{N} \left(\Phi_{i,model} - \Phi_{i,exp}\right)^2 \tag{25}$$

where $N$ represents the number of data points in the experimental profile and $\Phi_{i,model}$ and $\Phi_{i,exp}$ stands for the numerical and experimental values at point $i$, respectively. Any point at which no information was available for one or more of the simulations results taken from the literature was disregarded. Then, in order to provide a relative ranking between the different simulation approaches, a normalization of the $Error_{model}$ by the minimum value of the $Error_{model}$ obtained among the different models was applied, namely:

$$Mark^{\Phi}_{model} = \frac{Error^{\Phi}_{model}}{\min\left[Error^{\Phi}_{model}\right]} \tag{26}$$

So, for each of the three measurements stations, each model was attributed one mark per variable e.g. a total of five marks per measurements station and per model. Then, by adding the fifteen different marks attributed to each model, a total score is obtained for each model and can be used to rank them. The best achievable score was therefore 15 but it is important to specify though that even in such a (improbable) case, the ranking would remain relative e.g. it would not indicate that the corresponding model should be considered as being intrinsically perfect but simply that it outperformed all the other considered models for the selected measurements stations and variables.

Table 2: Scoring of the different simulations results.

| Position | Variable | RSM_1 | RSM_2 | PANS | LES | SAS |
|---|---|---|---|---|---|---|
| $x = 0\ mm$ | $U$ | 1.22 | 3.57 | 1.99 | **1.00** | 1.66 |
| | $V$ | 1.72 | **1.00** | 2.01 | 1.22 | 1.33 |
| | $\overline{u''u''}$ | 1.62 | 1.78 | **1.00** | 1.08 | 1.78 |
| | $\overline{v''v''}$ | 1.63 | **1.00** | 2.38 | 2.63 | 1.59 |
| | $\overline{u''v''}$ | 1.13 | 1.47 | 2.68 | 3.55 | **1.00** |
| $x = 11\ mm$ | $U$ | 1.07 | 1.22 | 1.44 | 1.53 | **1.00** |
| | $V$ | 1.16 | **1.00** | 1.11 | 1.49 | 1.01 |
| | $\overline{u''u''}$ | 5.37 | 2.88 | **1.00** | 1.02 | 1.50 |
| | $\overline{v''v''}$ | 1.18 | **1.00** | 2.29 | 1.64 | 1.04 |
| | $\overline{u''v''}$ | 5.38 | **1.00** | 1.87 | 1.70 | 2.08 |
| $y = 0\ mm$ | $U$ | 1.07 | 1.85 | 1.18 | **1.00** | 1.85 |
| | $V$ | 1.48 | **1.00** | 1.93 | 1.30 | 1.20 |
| | $\overline{u''u''}$ | 1.55 | **1.00** | 1.28 | 1.31 | 1.09 |
| | $\overline{v''v''}$ | 2.07 | **1.00** | 2.67 | 3.04 | 2.51 |
| | $\overline{u''v''}$ | 1.19 | 1.25 | **1.00** | 1.12 | 1.02 |
| | **Total** | **28.84** | **22.01** | **25.84** | **24.64** | **21.67** |

As can be seen in Table 2, although the SST-SAS model hits the best mark only twice, compared to the "best" performer e.g. RSM_2 (with 8 hits), the much better homogeneity of the SST-SAS results finally gives it the first place, closely followed by RSM_2. The third place goes to LES, followed by PANS and RSM_1 in last position.

# 5 Conclusion

This paper has explored the capability of the SST-SAS model to predict the flow in a staggered tube bundle. The triple decomposition of the unsteady velocity field was adopted to obtain the total Reynolds stress tensor. The simulation results obtained with the SST-SAS model proved to be quite satisfactory when compared with the experimental data in terms of mean velocity and turbulence quantities. Furthermore, when quantitatively compared with simulations results representative of different modeling alternatives available in the literature, the SST-SAS model featured a remarkable homogeneity of the predictive capability of its results. Hence, the present study confirms that the SST-SAS model must be considered as a very good alternative to LES and not only because of its reduced computational requirements but also because of the intrinsically good predictive quality of the resulting simulations.

# Acknowledgments

This work has been supported for the Projects ECOSud-MINCyT "Etude numérique et expérimentale de l'écoulement du vent autour de reservoirs de combustible liquid", CONICET-PUE-IDIT, "Vulnerability of infrastructure and physical environment associated with fuel transportation and storage", FONCyT-PICT-2017 "Study of the structural vulnerability of fuel storage tanks and pipes due to loads generated by wind and explosions", National University of Córdoba "Development and application of theoretical, numerical, experimental and computational Codes in Fluid mechanics and chaotic intermittency" and the National University of Cuyo Project 06/B378, "Wind pressures on tanks and horizontal pipes close to the ground considering their interferences in the flow though numerical models". The first author has a Ph.D. fellowship from CONICET.

# References

Benhamadouche, S. and Laurence, D. (2003). LES, coarse LES, and transient RANS comparisons on the flow across a tube bundle. *International Journal of Heat and Fluid Flow*, 24:470–479.

Chaouat, B. (2017). The state of the art of hybrid RANS/LES modeling for the simulation of turbulent flows. *Flow Turbulence and Combustion*, 99:279–327.

Davidson, L. (2006). Evaluation of the SST-SAS model: channel flow, asymmetric diffuser and axi-symmetric hill. In *Proc. of ECCOMAS 2006, Egmond aan Zee, Netherlands.*

Duffal, V., de Laage de Meux, B., and Manceau, R. (2021). Development and validation of a new formulation of hybrid temporal large-eddy simulation. *Flow Turbulence and Combustion*, https://doi.org/10.1007/s10494-021-00264-z.

Egorov, Y. and Menter, F. (2008). Development and application of SST-SAS turbulence model in the DESIDER project. *Notes on Numerical Fluid Mechanics and Multidisciplinary Design*, 97:261–270.

ERCOFTAC-IAHR-Workshop (1993). 2nd ERCOFTAC-IAHR Workshop on Refined Flow Modelling. In *ERCOFTAC-IAHR*, Lisbon, Portugal.

ERCOFTAC-IAHR-Workshop (1994). 3nd ERCOFTAC-IAHR Workshop on Refined Flow Modelling. In *ERCOFTAC-IAHR*, UMIST (The University of Science and Technology in Manchester), Manchester, United Kingdom.

Fröhlich, J. and Von Terzi, D. (2008). Hybrid LES/RANS methods for the simulation of turbulent flows. *Progress in Aerospace Sciences*, 44(5):349–377.

Girimaji, S. (2006). Partially-averaged navier-stokes model for turbulence: a reynolds-averaged navier-stokes to direct numerical simulation bridging method. *Journal of Applied Mechanics*, 73:413–421.

Grioni, M., Elaskar, S., and Mirasso, A. (2018). Scale-Adaptive Simulation of flow around a circular cylinder near a plane boundary. *Journal of Applied Fluid Mechanics*, 11(6):1477–1488.

Grioni, M., Elaskar, S., and Mirasso, A. (2020). A numerical study of the flow interference between two circular cylinders in tandem by Scale-Adaptive Simulation model. *Journal of Applied Fluid Mechanics*, 13(1):169–183.

Hanjalić, K. and Launder, B. (2020). Eddy-Viscosity transport modelling: A historical review. In *50 Years of CFD in Engineering Sciences*, pages 295–316. Springer.

Hassan, Y. and Barsamian, H. (2004). Tube bundle flows with the large eddy simulation technique in curvilinear coordinates. *International Journal of Heat and Mass Transfer*, 47(14-16):3057–3071.

Johnson, R. W. (2008). Modeling strategies for unsteady turbulent flows in the lower plenum of the vhtr. *Nuclear Engineering and Design*, 238(3):482–491.

Menter, F. (2015). Elements and applications of Scale-Resolving Simulation methods in industrial CFD. In Fröhlich, J., Kuerten, H., Geurts, B., and Armenio, V., editors, *Direct and Large-Eddy Simulation IX*, volume 20 of *ERCOFTAC Series*, pages 179–195. Springer, Cham.

Menter, F. and Egorov, Y. (2005). A scale adaptive simulation model using two-equation models. *AIAA Paper 2005-1905*, pages 1–13.

Menter, F. and Egorov, Y. (2006). Revisiting the turbulent scale equation. In *IUTAM Symposium on One Hundred Years of Boundary Layer Research*, pages 279–290. Springer.

Menter, F. and Egorov, Y. (2010). The scale-adaptive simulation method for unsteady turbulent flow predictions. part 1: theory and model description. *Flow, Turbulence and Combustion*, 85(1):113–138.

Menter, F., Kuntz, M., and Bender, R. (2003). A scale-adaptive simulation model for turbulent flow predictions. *AIAA Paper 2003-0767*, pages 1–11.

Menter, F. R. (1994). Two-equation eddy-viscosity turbulence models for engineering applications. *AIAA Journal*, 32:1598–1605.

Menter, F. R., Gritskevich, M. S., and Schtze, J. (2012). Global vs. zonal approaches in hybrid RANS-LES turbulence modelling progress in hybrid rans-les modelling. *Notes on Numerical Fluid Mechanics and Multidisciplinary Design*, 117:15–28.

Minelli, G., Krajnović, S., and Basara, B. (2017). LES and PANS of turbulent flow through a staggered tube bundle. In *Fluids Engineering Division Summer Meeting*, volume 58059, page V01BT12A009. American Society of Mechanical Engineers.

Moulinec, C., Pourquie, M., Boersma, B., Buchal, T., and Nieuwstadt, F. (2004). Direct numerical simulation on a cartesian mesh of the flow through a tube bundle. *International Journal of Computational Fluid Dynamics*, 18(1):1–14.

Patankar, S. V. and Spalding, D. B. (1972). A calculation procedure for heat, mass and momentum transfer in three-dimensional parabolic flows. *International Journal of Heat and Mass Transfer*, 15:1787–1806.

Paul, S., Ormiston, S., and Tachie, M. (2008). Experimental and numerical investigation of turbulent cross-flow in a staggered tube bundle. *International Journal of Heat and Fluid Flow*, 29(2):387–414.

Ridluan, A. and Tokuhiro, A. (2008a). Benchmark simulation of turbulent flow through a staggered tube bundle to support CFD as a reactor design tool. part I: SRANS CFD simulation. *Journal of nuclear science and technology*, 45(12):1293–1304.

Ridluan, A. and Tokuhiro, A. (2008b). Benchmark simulation of turbulent flow through a staggered tube bundle to support CFD as a reactor design tool. part II: URANS CFD simulation. *Journal of nuclear science and technology*, 45(12):1305–1315.

Rollet-Miet, P., Laurence, D., and Ferziger, J. (1999). LES and RANS of turbulent flow in tube bundles. *International Journal of Heat and Fluid Flow*, 20(3):241–254.

Rotta, J. (1972). Turbulente strömungen. *Teubner, Stuttgart*.

Simonin, O. and Barcouda, M. (1986a). Flow through staggered tube bundle - ERCOFTAC Classic Collection Database. http://cfd.mace.manchester.ac.uk/ercoftac/doku.php?id=cases:case078.

Simonin, O. and Barcouda, M. (1986b). Measurements of fully developed turbulent flow across tube bundle. In *Proc. Third Int. Symp. Applications of Laser Anemometry to Fluid Mechanics, Lisbon, Portugal*.

Simonin, O. and Barcouda, M. (1988). Measurements and prediction of turbulent flow entering a staggered tube bundle. In *Proceedings of Fourth International Symposium on Applications of laser anemometry to fluid mechanics, Lisbon, Portugal*.